Title: **Sodium channel endocytosis drives axon initial segment plasticity**

Short title: Sodium channel internalization tunes neuronal output.

Authors

Amélie Fréal[1,2]*†, Nora Jamann[1,2], Jolijn Ten Bos[2], Jacqueline Jansen[2], Naomi Petersen[1], Thijmen Ligthart[1], Casper C. Hoogenraad[2,3], Maarten H. P. Kole[1,2]*

Affiliations

[1] Axonal Signaling Group, Netherlands Institute for Neurosciences (NIN), Royal Netherlands Academy for Arts and Sciences (KNAW); Amsterdam, The Netherlands,

[2] Cell Biology, Neurobiology and Biophysics, Department of Biology, Faculty of Science, Utrecht University; Utrecht, The Netherlands,

[3] Department of Neuroscience, Genentech, Inc; South San Francisco, United States,

*Corresponding authors. Email: m.kole@nin.knaw.nl and a.freal@vu.nl

† Present address: Department of Functional Genomics, Vrije Universiteit (VU) Amsterdam, The Netherlands

Abstract

Activity-dependent plasticity of the axon initial segment (AIS) endows neurons with the ability to adapt action potential output to changes in network activity. Action potential initiation at the AIS highly depends on the clustering of voltage-gated sodium channels, but the molecular mechanisms regulating their plasticity remain largely unknown. Here, we developed genetic tools to label endogenous sodium channels and their scaffolding protein, to reveal their nanoscale organization and longitudinally image AIS plasticity in hippocampal neurons in slices and primary cultures. We find that NMDA receptor activation causes both long-term synaptic depression and rapid internalization of AIS sodium channels within minutes. The clathrin-mediated endocytosis of sodium channels at the distal AIS increases the threshold for action potential generation. These data reveal a fundamental mechanism for rapid activity-dependent AIS reorganization and suggests that plasticity of intrinsic excitability shares conserved features with synaptic plasticity.

Teaser

Rapid activity-dependent sodium channel internalization at the axon initial segment tunes the action potential output.

MAIN TEXT

Introduction

The axon initial segment (AIS) is a critical domain of all excitable neurons which maintains neuronal polarity and functionally acts as the final synaptic integration site for action potential (AP) generation (*1, 2*). The threshold and upstroke dynamics of neuronal APs rely, in part, on the specific distribution, density, and isoforms of voltage-gated sodium (Na_V) channels expressed along the AIS. The AIS localization of $Na_V1.2$ and $Na_V1.6$ channels, the two main isoforms of Na_V channels in excitatory neurons is mediated by the interaction with the AIS scaffold protein Ankyrin G (AnkG) (*3, 4*). Over the last decade emerging evidence showed that AIS morphology changes with activity in a brain region- and cell type-dependent manner. *In vivo* experiments demonstrated that changes in sensory input streams induce bidirectional changes of AIS length with temporal scales of one hour to several weeks, mediating a homeostatic plasticity of action potential output (*5-7*). AIS plasticity varies from subtle changes in ion channel isoform expression (*8*), to relocation of the AIS along the axis of the axonal membrane (*9*), changes in AIS length (*6*) or to a complete proteolysis of AIS proteins during excitotoxicity (*10-12*). However, in contrast to the detailed understanding of the mechanisms regulating synaptic plasticity (*13*), the specific molecular mechanisms controlling AIS plasticity are far from being understood. A comprehensive molecular model for how AIS plasticity is induced and expressed is still lacking. Molecular players implicated in activity-dependent AIS relocation include L-type voltage-gated calcium (Ca^{2+}) channels, calcineurin, myosin II/phospho-myosin light chain, and/or the AKT-ULK1 pathway (*9, 14-19*). A major limitation in our understanding of AIS plasticity mechanisms is that they mostly have been studied by comparing the AIS across large populations of differentially treated neurons. Live reporters allowing longitudinal analysis of AIS structure without affecting its organization and function are still lacking (*20, 21*). Moreover, while most studies have focused on the scaffold protein AnkG, little is known about the redistribution of Na_V channels during plasticity. During AIS development, two main trafficking routes have been reported for membrane proteins. They are either inserted into the somatic and/or axonal membrane before diffusing laterally until they get immobilized at the AIS, like Neurofascin-186 and the voltage-gated potassium channel $K_V7.3$ (*22*), or they are directly targeted into the AIS membrane, as has been shown for $Na_V1.6$ channels (*23*). Nevertheless, in both cases, their stable accumulation at the AIS depends on the local inhibition of their internalization by the interaction with AnkG and adaptor proteins (*24-26*). Here, we hypothesized that, during activity-dependent AIS plasticity, the membrane

channel reorganization is mediated by the dynamic trafficking of Na_V1 channels. To resolve the molecular events underlying AIS plasticity, we took advantage of a newly developed knock-in mouse line expressing green fluorescent protein (GFP)-labelled AnkG (*27*) and used the ORANGE CRISPR/Cas9 system (*28*) to tag endogenous Na_V1 channels, allowing the interrogation and live imaging of the molecular signaling pathways during activity-induced structural plasticity of the AIS.

Results

NMDAR activation induces both synaptic depression and AIS plasticity

To image the AIS of individual pyramidal neurons in real time we took advantage of a recently generated AnkG-GFP knock-in mouse line and performed bilateral injections with AAV5-CamKII-Cre into the hippocampal CA1 area to obtain Cre-dependent expression of AnkG-GFP from the calmodulin-dependent kinase II (CaMKII) promotor (**Fig. 1A,** (*27*)). Confocal imaging in acute hippocampal slices showed that AnkG-GFP fluorescence was detectable in the proximal axon of pyramidal neurons along the pyramidal layer (**Fig. 1B**), and the GFP signal colocalized with the AIS markers AnkG, β4-spectrin (**fig. S1A**) and $Na_V1.6$ (n = 10 AIS, **fig. S1B**). To induce activity-dependent plasticity we modified a previously developed approach for chemical long-term synaptic depression and exposed acute slices to the N-methyl-D-aspartate (NMDA) receptor agonist NMDA (*29*). When 20 µM NMDA was applied for 3 min, rapidly followed by the NMDAR-selective antagonist 2-amino-5-phosphonovaltuderic acid (APV, 100 µM, 5 min), we observed a strong membrane depolarization causing transient action potential firing (on average 4.11 ± 1.35 min, n = 14) but not with APV alone (Control, **Fig. 1C**), enabling correlating AnkG-GFP imaging during changes of neuronal network activity. Stimulation of the Schaffer collaterals (SC) and recording the evoked excitatory postsynaptic currents (EPSCs) from CA1 pyramidal neurons confirmed that NMDA exposure caused LTD (at 60 min, on average ~30% peak EPSC amplitude reduction in NMDA vs ~6% in Control, **Figs. 1B,D**). Interestingly, when we simultaneously imaged AnkG-GFP fluorescence during NMDA application we observed a significant decrease in AIS length already at 30 min ($p < 0.0001$, and at 60 min on average 15% or ~4.75 µm length reduction, $p < 0.0001$, **Fig. 1E,F**). Such rapid AnkG shortening is consistent with recent longitudinal imaging of AnkG-GFP in this mouse line (*27*). Also, the distance of the AIS start relative to the soma was increased in the NMDA group (**fig. S1C**, $p < 0.01$, ~3 µm), suggesting that both the proximal and distal regions of the AIS are putative sites of plasticity (**fig. S1C**). In control imaging sessions (APV alone) no AIS shortening was observed, excluding technical confounding factors by AnkG-GFP imaging or whole-cell recordings (p =

0.13, 0 vs. 60 min, **Fig. 1F**). Furthermore, in separate experiments when we examined the effects of NMDA application on AIS length in acute slices not used for electrophysiological recordings or live imaging, β4-spectrin staining confirmed that NMDA induced a 9% shortening of the AIS within 30 min (n > 200 neurons per condition**, fig. S1D**). Finally, in control experiments applying APV before, during and after NMDA application neither LTD nor AIS plasticity was triggered (**Fig. S1 E,F**).

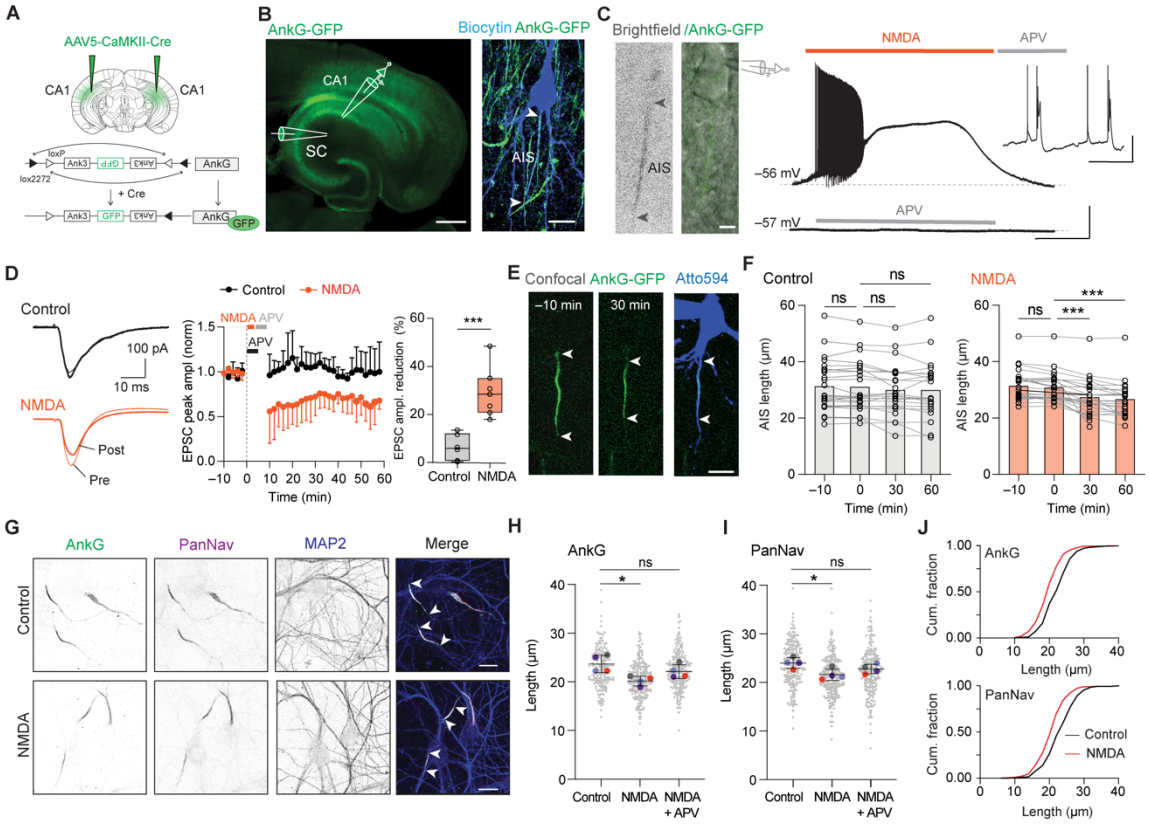

Fig. 1. NMDAR activation induced AIS shortening in acute hippocampal slices and cultured neurons.

(**A**) Strategy to induce expression of AnkG-GFP in CA1 pyramidal neurons (**B**) Image of hippocampal AnkG-GFP and patch-clamp configuration stimulating Schaffer collaterals (SC) and CA1 neuron filled with biocytin and immunostained against GFP. Scale bars, 500 µm and 15 µm. (**C**) *Left*, live imaging of AnkG-GFP and brightfield image during whole-cell recording. *Right top*, application of 20 µM NMDA followed by APV ('NMDA') induces action potential burst firing. *Right bottom*, APV alone ('Control') does not change resting potential. Scale bars, 10 µm; 1 min, 30 mV; 50 ms, 30 mV (inset). (**D**) Example EPSC traces before (pre) and after 60 min (post) control or NMDA treatment. NMDA causes LTD (NMDA, $n = 6$, control, $n = 7$, unpaired t-test ***$p < 0.001$). (**E**) Neuron filled with Atto594 and positive for AnkG-GFP before and after NMDA. White arrows indicate AIS start and end. Scale bar, 10 µm. (**F**) NMDA significantly reduces AIS length (Mixed effect analysis: control, $p = 0.0254$, NMDA, $p < 0.0001$. Šídák's multiple comparisons test, control: $p > 0.05$ for 0 vs –10, 30 and 60, NMDA: –10 vs 0, ns $p = 0.06$, 0 vs 30 ***$p < 0.001$, 0 vs 60 ***$p < 0.001$. control: $n = 24$, 16 whole-cell, 8 imaging, NMDA: $n = 25$, 14 whole-cell, 11 imaging). (**G**) Immunostaining of AnkG, PanNav and MAP2 in hippocampal neurons in control and after NMDA (4 min, 50 µM NMDA). Scale bar, 20 µm. **H-I**: AnkG (**H**) and PanNav (**I**) lengths in indicated conditions ($N = 4$ cultures, n > 440 neurons per condition). Matched Friedman test with Dunn's multiple comparisons test. AnkG, NMDA * $p = 0.027$, NMDA+APV $p = 0.96$

(ns). PanNav, NMDA *p = 0.027, NMDA+APV p = 0.15 (ns). (**J**) Cumulative fraction plots for AnkG and PanNav lengths.

Next, we examined NMDAR-mediated AIS plasticity in cultured hippocampal neurons. We treated DIV14 neurons with 50 µM of NMDA (4 min) and determined the AIS length after 30 min recovery compared to control cultures (no NMDA). We observed a significant reduction of AnkG (~20%) and total Na_V population (PanNav) (~10%) length respectively (**Fig. 1G-J**), which was blocked by APV (100 µM, 3 min before and during NMDA, **Fig. 1H,I**). These results are consistent with the findings obtained in acute slices. A leftward shift in the cumulative distribution plots indicated that the NMDA-induced shortening triggered a global reduction in length of the AIS in all neurons rather than a strong reduction in a subpopulation (**Fig. 1J**). Together, these data show that brief NMDA application, which causes a phasic increase in action potential firing and triggers synaptic LTD, is also associated with the robust and rapid shortening of the AIS, both in hippocampal acute slices and cultured neurons.

Loss of Nav following NMDAR activation specifically occurs in the distal AIS

The AIS of hippocampal excitatory neurons contains both sodium channel isoforms $Na_V1.2$ and $Na_V1.6$ (*30*). To test whether NMDA-induced AIS plasticity selectively affects one or both isoforms, we first characterized their distribution along the AIS in primary cultured neurons.

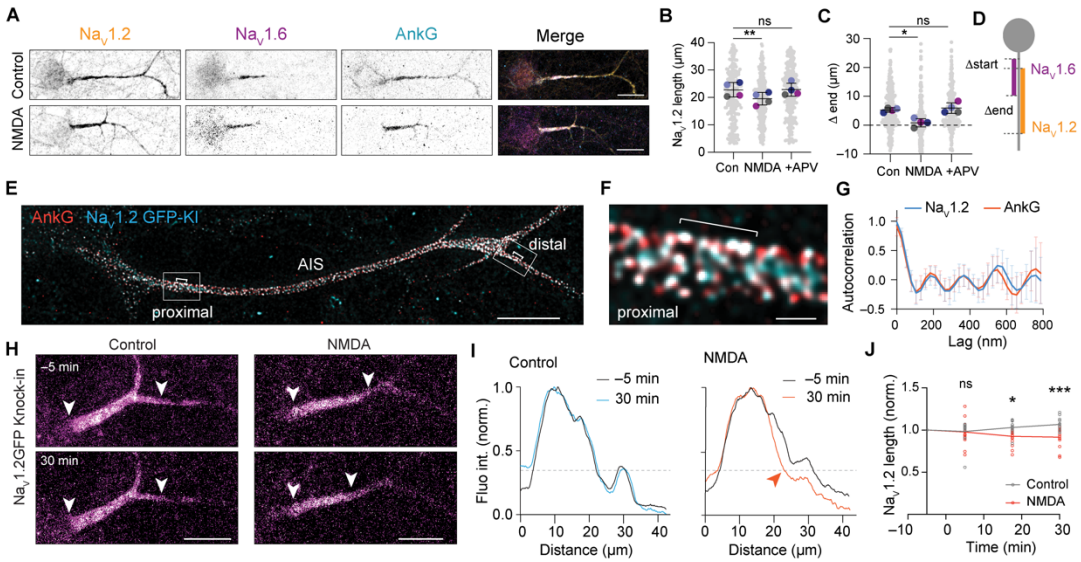

Fig. 2. $Na_V1.2$ is selectively reduced in the distal AIS during NMDAR-mediated plasticity. (**A**) Immunostaining for $Na_V1.2$, $Na_V1.6$ and AnkG on DIV14 in control and NMDA. Scale bars, 20 µm. (**B**) Average length of AIS $Na_V1.2$ reduced by NMDA exposure and blocked by APV (NMDA+APV). Repeated-measures One-Way ANOVA with Dunnett's multiple comparisons test, NMDA, **p = 0.008, NMDA+APV, ns p = 0.99. *N* = 4 cultures with at least 236 neurons per condition. (**C, D**) NMDA-mediated reduction in D end ($Na_V1.2$–$Na_V1.6$). (C) Repeated-measure One-way ANOVA with Dunnett's multiple comparisons test, *N* = 4 cultures. NMDA, *p = 0.022, NMDA+APV, ns p = 0.76. At least 260 neurons per condition, and corresponding scheme (D). (**E, F**) STED image of DIV14 $Na_V1.2$-GFP knock-in neuron stained for GFP and AnkG with zoom in of the proximal AIS. Scale bars 5 µm and 500

nm (zoom). (**G**) Autocorrelation of AnkG and $Na_V1.2$ fluorescence profiles in the proximal AIS, $n = 8$ neurons. (**H**) Live-cell imaging of $Na_V1.2$-GFP knock-in neuron 5 min before and 30 min after NMDA and control. Scale bars, 10 µm. White arrowheads point to start and end of $Na_V1.2$-GFP signal. (**I**) Corresponding fluorescence intensities normalized and smoothened over 1 µm. Dashed lines delineate the thresholds of end position, and red arrow points at the distal shortening 30 min after NMDA. (**J**) Average $Na_V1.2$-GFP length of control neurons (gray, $n = 13$ neurons in $N = 2$ cultures) or in NMDA condition (red, $n = 15$ in $N = 2$ cultures) normalized to the first frame. Mixed-effects analysis with Šídák's multiple comparisons test, 5 min, ns $p > 0.99$; 17.5 min, *$p = 0.019$; 30 min, ***$p = 0.0009$.

Staining of DIV14 hippocampal neurons revealed that 90% and 80% of AnkG-positive AISs were also positive for $Na_V1.2$ and $Na_V1.6$ respectively, with $Na_V1.2$ expressed along the entire AIS, whereas $Na_V1.6$ was predominantly found in the proximal AIS (**fig. S2A**). At DIV21 $Na_V1.6$ expression became more prominent in comparison to $Na_V1.2$ (**fig. S2B–D**). In DIV14 cultures, brief application of NMDA significantly reduced the length of $Na_V1.2$, but not $Na_V1.6$ (**Fig. 2A,B** and **fig. S3B**), by 14% compared to control condition in ~75% of the experiments ($n = 21$ cultures), which was blocked by APV (**Fig. 2B**).

We compared the intensity and the integrated intensity of Na_V1 isoform staining after NMDA application, normalized to the control condition in each experiment. While neither $Na_V1.6$ staining mean intensity nor density changed after NMDA exposure, $Na_V1.2$ staining density was reduced by 25%, with no change in the mean intensity (**fig. S3A-C**). These findings suggest that the NMDAR-induced shortening may reflect a local channel removal rather than a global loss of $Na_V1.2$ channels. We did not detect a shift of the AIS along the axon; the absolute start position of both $Na_V1.2$ and $Na_V1.6$ remained unaltered (**fig. S3D**). To further explore the location of NMDAR-induced changes we next measured $Na_V1.2$ and $Na_V1.6$ relative start and end positions to determine the location of AIS shorting (**Fig. 2C,D** and **fig. S3E**). NMDAR activation changed the relative start positions of $Na_V1.6$ and $Na_V1.2$ (~2.2 µm reduction) and strongly impacted the relative end positions (~5 µm reduction), suggesting that the length reduction of the AIS occurs at both extremities, but mostly reflects changes at the distal end of the AIS (**Fig. 2C**).

To better and more directly monitor $Na_V1.2$ channel membrane dynamics in living cells without over-expression artefacts, we used the ORANGE CRISPR/Cas9 system to fluorescently tag the endogenous $Na_V1.2$ channel (*28*). Insertion of GFP in the C-terminal part of the channel revealed a strong enrichment of $Na_V1.2$ at the AIS, while lower GFP levels could be detected in the distal axon and somato-dendritic compartment, (**fig. S4A)** as previously reported (*31*). Using STED microscopy, we observed a colocalization of AnkG with $Na_V1.2$ (GFP) adopting a ring-like organization throughout the AIS (**Fig. 2E,F** and **fig. S4C**). The auto-correlation analysis revealed a highly periodic arrangement of the two proteins, both in the proximal and distal AIS

(**Fig. 2G** and **fig. S4D-F**) with a similar peak-to-peak distance of ~190 nm (**fig. S4F**), as previously observed for $Na_V1.2$ and $Na_V1.6$ and for AnkG (*31, 32*). Moreover, NMDA application caused a ~10% reduction in the length of $Na_V1.2$-GFP signal (**fig. S4A,B**), indicating that our tagging approach does not impair $Na_V1.2$ channel behavior during plasticity.

We then performed time-lapse imaging of endogenous $Na_V1.2$-GFP before, during and after NMDA application (**Fig. 2H-J**) and observed a loss of GFP fluorescence after 30 min, specifically in the distal AIS (**Fig. 2H,I**). Notably, the average normalized GFP length was already significantly reduced at 17.5 min after incubation with NMDA (~10% reduction, **Fig. 2J**). The comparison of $Na_V1.2$ start and end positions before and after further confirmed a selective and significant reduction of $Na_V1.2$ expression at the distal AIS (**fig. S4G**). Altogether, our data show converging lines of evidence for a rapid NMDAR-dependent remodeling of the AIS, mostly affecting distally localized $Na_V1.2$ channels. The greater degree of plasticity in this subcellular domain implies the presence of specific mechanisms initiated by NMDAR activation and locally controlling Na_V isoform distribution.

Synaptic NMDAR-mediated depolarization triggers AIS plasticity

Although some studies reported the presence of NMDARs at axonal presynaptic release terminals (*33*), they are typically not present at the AIS (*34*). To unravel the precise localization of NMDARs in DIV14 primary hippocampal neurons we used ORANGE to extracellularly tag the endogenous obligatory NMDAR subunit GluN1 with GFP (*28*) (**Fig. 3A,B**). We first stained for GFP without permeabilization and only detected a very faint surface expression of GluN1 in the AIS of 50% of all neurons. When present at the AIS, membrane GFP signal only occupied 0.16% of AIS surface (~30-times lower than at dendritic membrane sites; 4.8% occupancy, **Fig. 3A,B**). A subsequent total GFP staining revealed a diffuse pattern in the neuron, including in the AIS, as well as bright and dense puncta in the postsynaptic density (**Fig. 3A** and **fig. S5A**). The low abundancy of NMDARs at the AIS suggests that the effect of NMDA application might be mediated via extrasynaptic or synaptic NMDARs at somato-dendritic sites. To test this idea experimentally, we used MK-801, blocking glutamate-bound NMDARs (*35, 36*), to distinguish between extrasynaptic and synaptic NMDAR contributions. MK-801 applied 5 min before and during NMDA application blocked the shortening of both AnkG and $Na_V1.2$, indicating that activation of synaptic NMDARs is required to trigger AIS plasticity (**fig. S5B,C**). Taken together, the absence of NMDARs inserted at the AIS membrane and the requirement of

activated NMDARs for the induction of AIS shortening reveals that the activation of synaptic NMDAR is the trigger for rapid AIS plasticity.

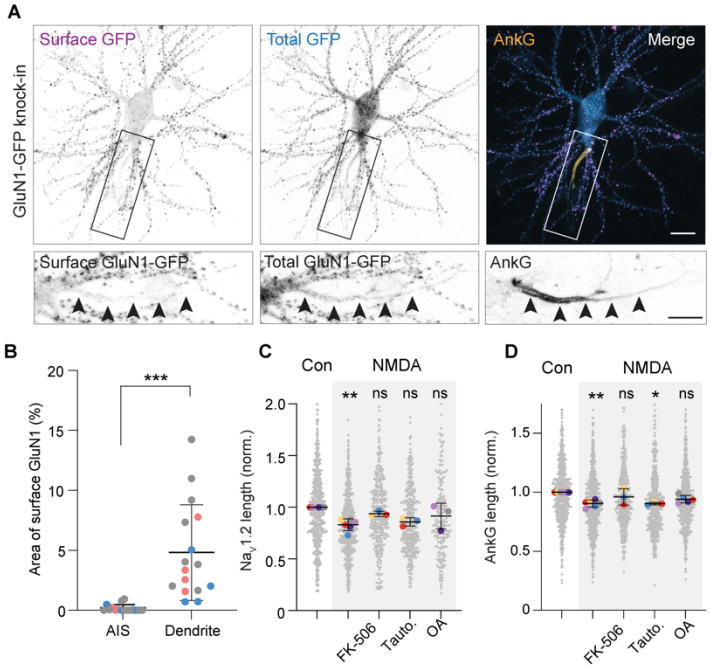

Fig. 3. AIS plasticity is triggered by the activation of synaptic NMDARs and relies on calcineurin.
(A) GluN1-GFP knock-in neurons stained for extracellular GFP, total GFP and AnkG. Scale bars are 15 µm and 10 µm in the zooms. Arrows show the trajectory of the AIS and axon. **(B)** Percentage of the AIS or dendrites surface positive for extracellular GFP. Wilcoxon's test, ***p = 0.001, *n* = 16 neurons from 3 independent cultures. (**C,D**) $Na_V1.2$ and AnkG relative lengths in NMDA and in the presence of FK-506, Tautomycetin (Tauto) or Okadaic Acid (OA). *N* = 3 to 6 cultures, Kruskal-Wallis test. For $Na_V1.2$, NMDA **p = 0.0024, FK-506 ns p = 0.93, Tauto ns p = 0.06, OA ns p = 0.82. For AnkG: NMDA **p = 0.004, FK-506 ns p = 0.99, Tauto *p = 0.015, OA ns p = 0.28.

Which signaling pathway links synaptic NMDAR activation with AIS plasticity? We observed that NMDA caused to a strong membrane depolarization with action potential generation lasting for several minutes as well as LTD in acute slices (**Fig. 1C,D**). To test whether induction of synaptic LTD alone suffices to drive AIS plasticity we performed experiments in which we evoked LTD electrically (e-LTD, SC stimulation, 900 pulses @1 Hz, **fig. S5D,E**). Although we observed strong LTD (~48% EPSC peak amplitude reduction vs 8% in control) we did not observe AIS length changes (**fig S5F,G**). To further examine the role of LTD in AIS plasticity we used a NMDAR-independent induction protocol for LTD based on mGluR activation with the agonist DHPG (*37*). The results showed that neither the length of AnkG, $Na_V1.2$ nor $Na_V1.6$ changed (**fig. S5H**). We next hypothesized that the postsynaptic depolarization and associated APs during NMDA application are required to trigger AIS plasticity. To test this conjecture directly, we reproduced the NMDA-induced depolarization intrinsically by injecting positive

DC current, keeping the neuron for ~5 min above threshold for AP firing and live image AnkG-GFP. The results showed that the AIS length remained constant (**fig. S5I**). Altogether the experimental results show that neither synaptic depression nor somatic AP generation causes AIS plasticity, leaving open the possibility that the combination of dendritic NMDAR activation and axosomatic firing is required to trigger NMDAR-mediated $Na_V1.2$ removal from the distal AIS.

Next, we sought to identify the molecular signaling cascade responsible for the rapid NMDAR-mediated AIS remodeling. Both LTD and NMDAR-induced intrinsic plasticity of CA1 pyramidal neuron firing cause activation of numerous phosphatases (*29, 38, 39*) and interestingly some of these have also been shown to be implicated in AIS plasticity, like calcineurin (*14*). To test the involvement of calcineurin and other phosphatases, we applied NMDA in the presence of diverse pharmacological inhibitors to assess their ability to prevent the shortening of $Na_V1.2$ and AnkG (**Fig. 3C,D**, respectively). Inhibiting calcineurin (FK-506, 50 mM) or PP2A (with low dose of Okadaic Acid, OA, 2 nM) blocked the shortening of both AnkG and $Na_V1.2$ induced by NMDAR activation. Inhibition of PP1 (Tautomycetin, 10 μM) prevented the shortening of $Na_V1.2$ but not of AnkG (**Fig. 3C,D**). Thus, these results show that dephosphorylation is an important process in the removal of $Na_V1.2$ at the AIS and reveal a common signaling pathways leading to the expression of LTD at synapses and the AIS after activation of NMDAR.

AIS shortening is mediated by clathrin-mediated endocytosis

How are Na_V channels removed from the distal AIS during NMDAR-mediated AIS plasticity? We pharmacologically inhibited common signaling pathways known to promote protein removal and/or degradation (**Fig. 4A,B**, and **fig. S6**). We first tested the role of calpains, a family of calcium-dependent proteases. Although calpains have been shown to be involved in stress-mediated AIS disassembly (*10, 11, 40-42*) inhibition with the selective calpain inhibitor MDL 28170 during induction of NMDAR-mediated plasticity neither blocked the ~15% shortening of $Na_V1.2$ nor AnkG (**Fig. 4A,B**). Since it was shown previously that AIS proteostasis can be modulated by local Ecm29-targeted proteasome (*43*) we then tested the role of proteasome-mediated degradation. Interestingly, application of NMDA in the presence of the proteasome-blocker MG-132 prevented the shortening of AnkG, but not $Na_V1.2$ (**Fig. 4A,B** and **fig. S6A**). Finally, we addressed the involvement of endocytosis in controlling $Na_V1.2$ re-distribution

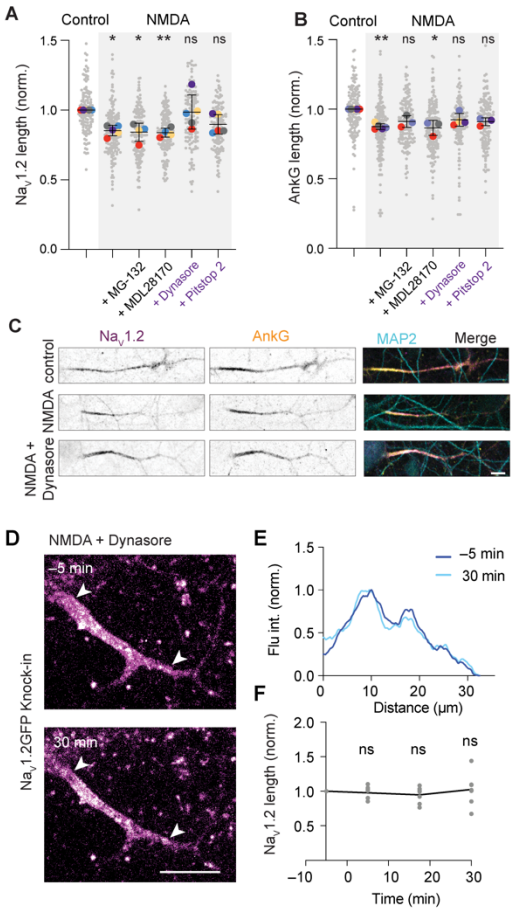

Fig. 4. Endocytosis is required for NMDA-induced Na$_V$1.2 removal from the AIS.
(**A**) Na$_V$1.2 and (**B**) AnkG relative length following NMDA application and in the presence of MG-132, MDL2870, Dynasore and Pitstop 2, N = 3-6 independent experiments and n >100 neurons per condition per experiment. Kruskal-Wallis test; NMDA: Na$_V$1.2 *p = 0.019, AnkG **p = 0.001, NMDA + MG-132: Na$_V$1.2 *p = 0.036, AnkG ns p = 0.21, NMDA + MDL28170: Na$_V$1.2 **p = 0.005, AnkG *p = 0.018, NMDA + Dynasore: Na$_V$1.2 ns p > 0.99, AnkG ns p = 0.38, NMDA + Pitstop 2: Na$_V$1.2 ns p = 0.068, AnkG ns p = 0.39. (**C**) Immunostaining for Na$_V$1.2, AnkG and MAP2 of DIV14 neurons in control conditions and NMDA with or without the dynamin inhibitor Dynasore. (**D**) Live-cell imaging of Na$_V$1.2-GFP knock-in neuron 5 min before and 30 min after NMDA treatment and control. Scales bars are 10 µm, white arrowheads point to the start and end point of the Na$_V$1.2-GFP signal. (**E**) Corresponding fluorescence intensities normalized to the maximum intensity. (**F**) Average Na$_V$1.2-GFP length of neurons treated with NMDA in the presence of Dynasore normalized to the first frame. Repeated-Measure one-way ANOVA with Šídák's multiple comparisons test, ns p > 0.70, n = 7 neurons in N = 2 cultures.

during plasticity. Na$_V$1.2 and Na$_V$1.6 channels have been reported to contain endocytic motifs which are important for their stabilization at the AIS membrane (*25, 44*). Consistent with these observations, the application of two distinct blockers for endocytosis, either by inhibiting dynamin GTPase activity (Dynasore, 80 µM) or clathrin (Pitstop 2, 20 µM), abolished the NMDA-induced shortening of Na$_V$1.2 and AnkG (**Fig. 4A-C, Fig. S6A, B**). To further corroborate this result in live neurons, we imaged individual Na$_V$1.2-GFP knock-in neurons live before and after the application of NMDA in the presence of Dynasore. Na$_V$1.2 length remained

unchanged, confirming that blocking dynamin prevents NMDA-induced AIS plasticity (**Fig. 4E,F**). We verified that none of these drugs alone affect AnkG nor $Na_V1.2$ lengths at the population level (**fig. S6B**), and that incubation with Dynasore alone during live imaging does not trigger AIS lengthening (**fig. S6C**). Altogether our results show that endocytosis is required for NMDAR-dependent AIS plasticity.

Recruitment of endocytic structures at the AIS during rapid plasticity

The reduction of $Na_V1.2$ channels during plasticity could be mediated by local endocytosis at the AIS or by lateral diffusion before internalization. To address the involvement of endocytosis during AIS plasticity, we first assessed the presence at the AIS of two members of the endocytic machinery, dynamin2 and clathrin light chain using CRISPR/Cas9 GFP knock-ins (*28*). We detected GFP puncta throughout the transfected neurons including at the AIS, stained with $Na_V1.2$ (**Fig. 5A**, **fig. S7A**). To visualize the putative internalization of $Na_V1.2$ channels after NMDA treatment we performed live imaging of neurons overexpressing dynamin2-GFP and $Na_V1.2$-mCherry. We first verified that overexpressed channels behave as endogenous channels in response to NMDA treatment. Live imaging of $Na_V1.2$-GFP showed that GFP length remained constant in control conditions while it significantly decreased 30 min after NMDA application (**fig. S7D,E** cf. **Fig. 2**). Dual-color live imaging of $Na_V1.2$-mCherry and dynamin2-GFP at various time points after NMDA application allowed us to visualize a few events at the AIS where dyamin2-GFP progressively localized to circular structures of $Na_V1.2$-mCherry, while $Na_V1.2$ signal progressively disappeared (**Fig. 5C,D**). However, as endocytosis is a fast process and happens at discrete locations, it was difficult to catch these events. We therefore decided to quantify the recruitment of dynamin-positive endocytic structures at the AIS following NMDA application in the presence of Dynasore. Dynasore inhibits the GTPase activity of dynamin thus only prevents the fission of endocytic pits but does not block the initiation of new clathrin-coated pits (*45, 46*). Applying Dynasore during NMDA treatment and the recovery time allowed us to visualize endocytic structures which formed during AIS plasticity. Indeed, we observed a significant increase of the relative surface area covered by dynamin2-GFP at the AIS (~1.5 fold), and of the average cluster area in the NMDA condition (~1.5 fold) in the presence of Dynasore (**Fig. 5A,B**, **fig. S7C**). No change was detected in the pattern of clathrin light chain (**fig. S7B**). To characterize those dynamin2 structures with higher spatial resolution, we performed STED imaging on neurons co-expressing dynamin2-GFP and $Na_V1.2$-mCherry. At the nanoscale, dynamin2 organized in two different patterns. Dynamin2

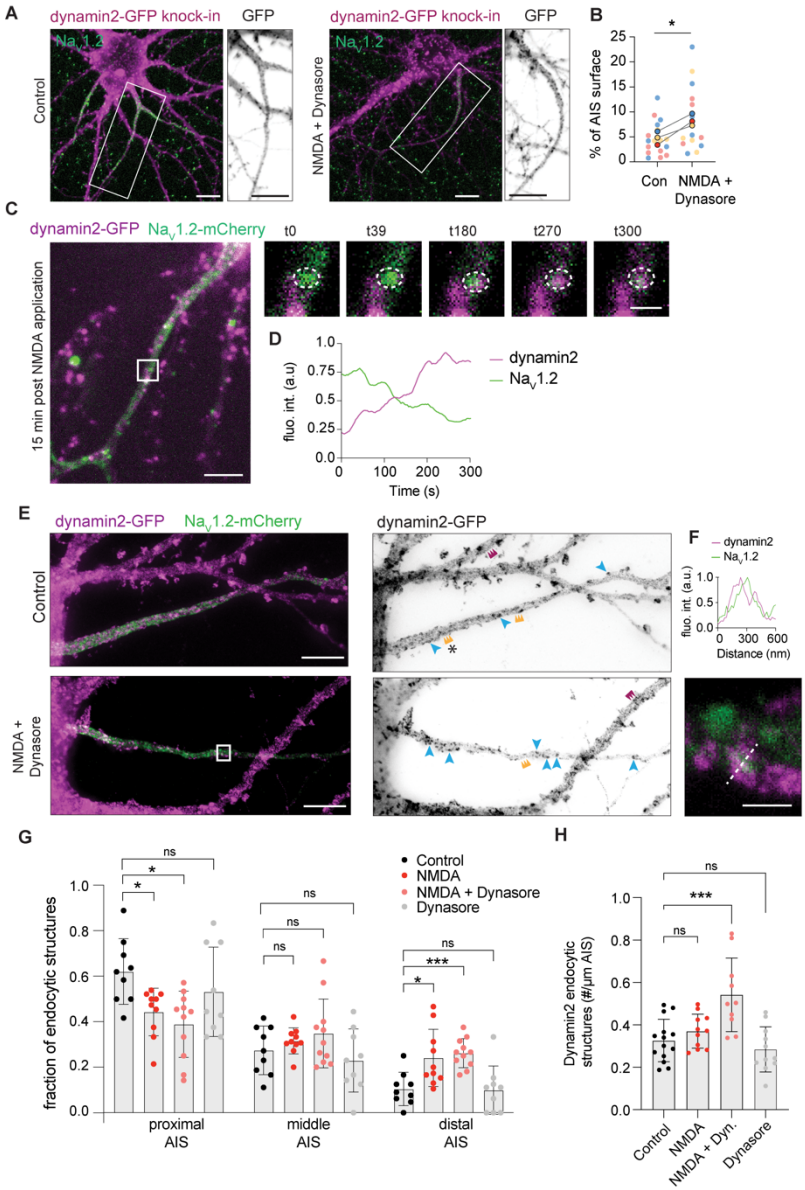

Fig. 5. Recruitment of the endocytic machinery at the AIS during rapid plasticity.

(**A**) Immunostaining for dynamin2 GFP knock-in reveals increased NMDA-induced dynamin clusters in the AIS. Scale bars, 10 µm. (**B**) Population analysis of dynamin2 surface in the $Na_V1.2$-positive AIS in indicated conditions. paired t-test, *p = 0.033. N = 3 independent experiments, 4 to 7 neurons per condition per experiment. (**C**) Simultaneous dual-color live imaging of a neuron co-expressing dynamin2-GFP and $Na_V1.2$-mCherry 15 min post NMDA treatment. Time points (in seconds) of the boxed areas are presented. Scale bars are 5 mm (left) and 500 nm (zooms). (**D**) Average fluorescence intensity inside the circle over time, smoothened over 24 s. (**E**) STED images of neurons co-expressing dynamin2-GFP and $Na_V1.2$-mCherry in indicated conditions. Scale bar 5 mm, blue arrowheads point at endocytic structures, colored combs show regions with periodic distribution of dynamin2 in the AIS (orange) or dendrites (magenta). (**F**) Zoom of the boxed area and fluorescence intensity profile along the dashed line. Scale bar 250 nm. (**G**) Distribution of dynamin2 endocytic structures along the AIS in indicated conditions. 2-way ANOVA with Tukey's multiple comparison test. Proximal AIS: Control vs NMDA *p = 0.015, Control vs NMDA + Dynasore *p = 0.037, Control vs Dynasore ns p = 0.69. Middle AIS: Control vs NMDA ns p= 0.58, Control vs NMDA + Dynasore ns p = 0.73, Control vs Dynasore ns p = 0.86. Distal AIS: Control vs NMDA ***p= 0.0006, Control vs NMDA + Dynasore *p = 0.047, Control vs Dynasore ns p = 0.99, $n > 9$ neurons from 2 independent experiments. (**H**) AIS Density of dynamin2 endocytic structures in indicated conditions. One-way ANOVA with Dunnett's multiple

comparison test. Control vs NMDA ns p = 0.68, Control vs NMDA + Dynasore ***p = 0.0002, Control vs Dynasore ns p = 0.72, *n* > 9 neurons from 2 independent experiments.

showed a periodic distribution in numerous regions of the axon and dendrites of control neurons (**Fig. 5E**, combs and **fig. S7F**). Although it was less regularly organized than actin and spectrins (*47, 48*), the analysis of the autocorrelation profile of dynamin2 fluorescence intensity revealed a periodicity of ~230 nm (**fig. S7F,G**). This indicates that dynamin2 might be part of the axonal submembrane cytoskeleton locally. Moreover, dynamin2 also formed circular, O-shaped structures (**Fig. 5E**, blue arrowheads) of around ~220 nm of diameter (**fig. S7H**), resembling typical endocytic structures reported for clathrin and dynamin in dendrites of neurons and other cell types (*45, 46, 49*). We then characterized the distribution of dynamin2 endocytic structures along the AIS in various conditions (**Fig. 5G).** Control neurons showed a high proportion of endocytic structures in the proximal part of the AIS (~60%, **Fig. 5G**). Notably, application of NMDA caused a striking change by significantly increasing the fraction of endocytic structures in the distal AIS. This increase was also observed after NMDA treatment in the presence of Dynasore, but not following Dynasore treatment alone (**Fig. 5G**), suggesting that this change is associated with NMDAR-mediated AIS plasticity. Moreover, we detected a significant increase in the number of dynamin2 endocytic structures in the NMDA + Dynasore condition, consistent with a recruitment of the endocytic machinery at the AIS during rapid plasticity (**Fig. 5H**). In this condition, we were also able to detect $Na_V1.2$-mCherry signal within dynamin2 endocytic structures (**Fig. 5F**), further supporting the hypothesis that $Na_V1.2$ channels can be endocytosed at the AIS during plasticity.

Altogether, our data show that activity-dependent $Na_V1.2$ channel removal from the AIS membrane is driven by clathrin-mediated endocytosis. Our results further suggest that a pool of dynamin2-positive endocytic structures is recruited to and retained at the distal AIS during the process of activity-dependent plasticity. Moreover, these dynamin2 endocytic structures were associated with $Na_V1.2$ channels. While we do not exclude that $Na_V1.2$ channels could diffuse out of the AIS before being internalized, our data show that those channels can be endocytosed at the AIS during rapid plasticity.

Endogenous $Na_V1.2$ displays a higher mobility in the distal AIS

Since dynamin2-positive endocytic structures are distributed uniformly along the AIS following NMDA application, we wondered why the distal pool of $Na_V1.2$ channel is preferentially affected during plasticity. Previous studies show that the interaction of Na_V1 channels or Neurofascin-186 with the scaffold AnkG limits their membrane diffusion and locally prevents

their internalization (*22, 24, 44, 50*). Therefore, we assessed if local differences in $Na_V1.2$ anchoring in basal conditions could explain its preferential loss from the AIS distal region during plasticity. We first performed a detergent extraction experiment on live neurons to address the tethering of Na_V channels to the submembrane cytoskeleton (*51*) (**fig. S8A-C**). After extraction, we observed significantly shorter AIS when stained for AnkG (16 ± 1.2% reduction) as well as $Na_V1.2$ (26 ± 2.2%) and $Na_V1.6$ (17 ± 1.6%, **fig. S8A,B**). The analysis of $Na_V1.2$ and $Na_V1.6$ relative expression patterns revealed a large loss of $Na_V1.2$ after extraction specifically in the distal AIS (**fig. S8C**), indicating that the anchoring of this channel is less strong in this region. To test this observation with an alternative method, we performed fluorescence recovery after photobleaching (FRAP) experiments to measure the mobility of endogenously-tagged $Na_V1.2$-GFP in DIV14 neurons (**fig. S8D-E**). We bleached separate regions within the AIS to compare the recovery in the proximal *versus* the distal part. The results showed a significantly larger recovery (~10% average recovery after 45 min) in the distal AIS compared to the proximal region (~7%, **fig. S8F,G**). The fluorescence recovered from the distal axon to the AIS (**fig. S8E,** white arrows), suggesting that $Na_V1.2$ channel accumulation at the AIS arises from retrograde diffusion along the axon as previously reported for Neurofascin-186 and $K_V7.3$ (*22*). Comparisons of distal versus proximal recovery percentage for multiple experiments confirmed a significant ~1.5-fold higher mobility of $Na_V1.2$ in the distal AIS (**fig. S8G**), further highlighting local differences in $Na_V1.2$ anchoring properties. The reduced anchoring of $Na_V1.2$ channels in the distal AIS could thus explain why those channels are preferentially lost from the distal region of the AIS.

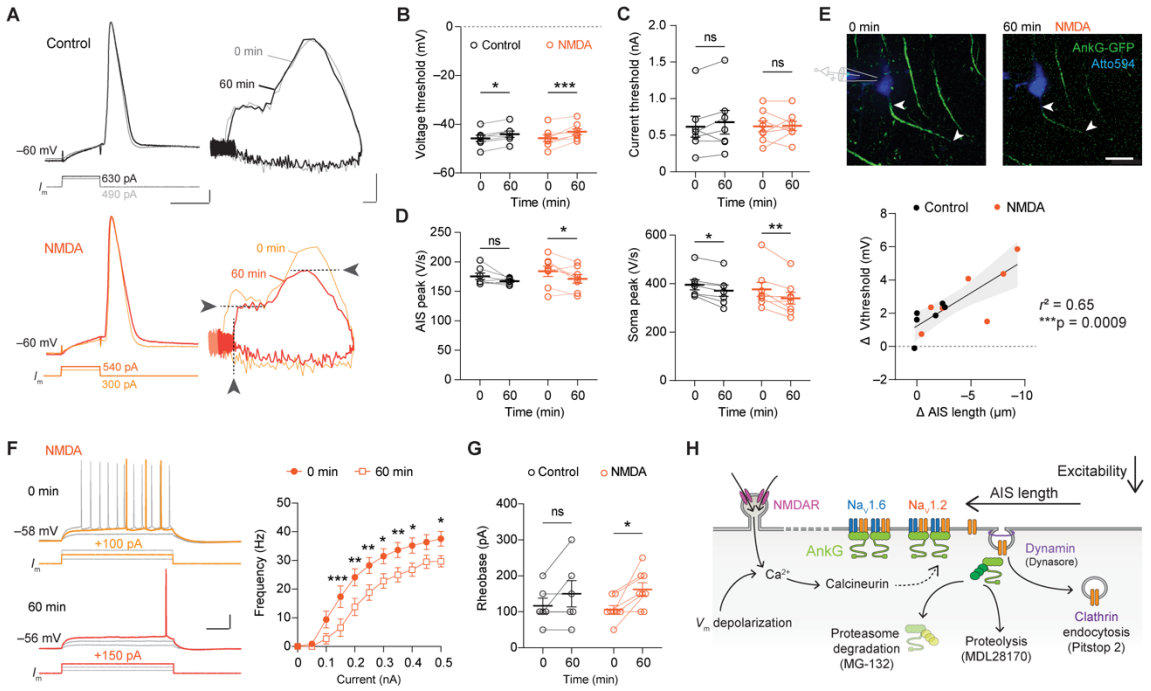

Fig. 6. NMDA-induced AIS shortening correlates with increased threshold for AP generation. (**A**) AP voltage-time traces and phase-plane plots, before and 60 min after NMDA or APV. Scale bars, 3 ms and 10 mV; 10 mV and 100 V/s. Black arrows show voltage threshold, AIS and soma peak rate-of-rise. (**B**) Voltage threshold significantly increased after 60 min (Two-way ANOVA p = 0.0001 (time), p = 0.78 (treatment), p = 0.278 (interaction). Šídák's multiple comparisons test, Ctrl 0 vs 60 *p <0.05, NMDA 0 vs 60 ***p < 0.001). (**C**) Current threshold was unaffected (2-way ANOVA p > 0.05). (**D**) NMDA reduces AIS and soma peak rate-of-rise. AIS peak, Two-way ANOVA p = 0.01 (time), p = 0.49 (treatment), p = 0.54 (interaction). Multiple comparisons tests, Ctrl 0 vs 60 p = 0.29 (ns), NMDA 0 vs 60 *p = 0.047. Soma peak, Two-way ANOVA p = 0.0005 (time), p = 0.48 (treatment), p = 0.40 (interaction). Multiple comparisons test Ctrl 0 vs 60 *p = 0.045, NMDA 0 vs 60 **p = 0.0028. (**E**) *Top*, AnkG-GFP imaging during NMDA treatment. White arrowheads show AIS shortening. *Bottom*, AIS length change predicts AP voltage threshold. Continuous line depicts linear regression with 95% confidence interval (shaded area). (**F**) NMDA significantly reduced the *I-f* curve. Two-way ANOVA p < 0.0001 (current), p < 0.0001 (treatment), p = 0.046 (interaction). Multiple comparisons tests for current steps; *p < 0.05, **p < 0.01, ***p < 0.001. Scale bars, 100 ms, 20 mV. (**G**) Rheobase current significantly increased after NMDA. Two-way ANOVA p = 0.97 (treatment), p < 0.007 (time), p = 0.41 (interaction). Multiple comparisons test Ctrl 0 vs 60 p = 0.25 (ns), NMDA 0 vs 60 *p = 0.017 (**H**) Proposed AIS plasticity model (see Discussion). A-G: Data are depicted as individual scatter and mean ± SEM.

NMDAR-mediated AIS length reductions increase the action potential threshold

A loss of distal $Na_V1.2$ channels is expected to be accompanied by intrinsic neuronal excitability changes since the distal AIS plays a critical role in the initiation of APs (*1, 52*). To test this, we recorded in acute slices from the AnkG-GFP mice, and monitored AP properties in CA1 pyramidal neurons during whole-cell recording and simultaneously imaged the AIS with a confocal spinning disk (every 5 minutes, **Fig. 6, movie S1 and S2**). In these experiments the resting membrane potential remained constant for one hour (paired 2-way ANOVA, p = 0.052

for time, p = 0.73 treatment, *n* = 15). Both in control and the NMDA-treated neurons the voltage- but not the current threshold for initiating an AP significantly increased (**Fig. 6A-C**). The maximum peak in the AP rate-of-rise, reflecting mostly somato-dendritic Na_V activation, was reduced in both control and NMDA groups suggesting that during these recordings also NMDA-independent changes occurred (**Fig. 6D**). When assessing the distinct components of the AIS and soma of the spike, however, the AIS component that produces the AP onset, was selectively and significantly reduced by NMDA application (~13 V/s reduction, **Fig. 6D**). To examine the contribution of the geometrical AIS length changes more directly we leveraged the simultaneous live AIS imaging and recording and plotted the AIS length change against the properties of the changes in AP. Interestingly, a linear regression of AIS length change revealed a significant and strong prediction of the AP voltage threshold change (p = 0.0009, *n* = 13, **Fig. 6E**). The NMDAR-induced AP voltage threshold change also temporally correlated with the AIS length change (**fig. S9A**). In addition, NMDA treatment not only increased the AP threshold during brief large current injections but also significantly reduced the firing probability assessed with current-frequency (*I-f*) curves with long-duration current injections (**Fig. 6F,G**) but not in control recordings (**fig. S9B**).

Together, these data suggest that the rapid endocytosis of $Na_V1.2$ channels during NMDAR-mediated AIS plasticity limits the intrinsic capacity for action potential generation.

Discussion

Endogenous labeling of Na_V channels (this study and (*31*)) and AnkG (*27*) allowed us to longitudinally image, without overexpression artefacts, central AIS proteins during activity-dependent plasticity. These tools enabled interrogation and identification of the mechanisms mediating AIS remodeling at high spatiotemporal resolution on a single cell level, while avoiding the variability of cell population analysis. Within minutes, the brief application of NMDA triggered structural AIS plasticity predominantly characterized by the loss of AnkG and $Na_V1.2$ channels along several micrometers of the distal AIS (**Fig. 2**). The signaling pathway was initiated by synaptic NMDARs and involved phosphatases such as calcineurin, and ultimately activated clathrin-mediated endocytosis (**Figs 3, 4**). Finally, we reported that dynamin2 was recruited at the distal AIS during the rapid remodeling of this region (model in **Fig. 6H**). Live imaging provided structure-function assessment within the same neuron showing

that AIS shortening at the micrometer scale predicts the changes in threshold behavior of the AP (**Fig. 6E**). Notably, the rapid disassembly of the distal AIS was not directly dependent on synaptic depression, since inducing LTD electrically or using DHPG was not sufficient to trigger AnkG shortening. However, NMDAR-induced LTD and AIS shortening did evolve on the same timescale and shared multiple molecular mechanisms, from the role of clathrin-dependent endocytosis in the removal of AMPARs from the PSD (*53, 54*), to the requirement of calcineurin-mediated dephosphorylation (*55, 56*). In future experiments it would be interesting to investigate whether calcineurin directly dephosphorylates $Na_V1.2$, and address how this affects $Na_V1.2$ binding to AnkG and membrane dynamics of the channel. $Na_V1.2$ bears an endocytic motif in the II-III loop, which is masked by the interaction with AnkG, and thereby could block the internalization of the channel at the AIS (*44*). Interaction with AnkG alone however, might not be sufficient to prevent internalization, as shown for the MAP1B-binding mutant $Na_V1.6$ channel, which is still capable to bind to AnkG, but accumulates less at the AIS membrane because it undergoes endocytosis (*25, 57*). Another mechanism that AIS shortening shared with synaptic LTD is the contribution of the ubiquitin proteasome degradation system (UPS), which controls PSD-95 and AKAP150 levels during LTD (*58, 59*). Similarly, we observed that that blocking the UPS prevents the shortening of AnkG following NMDA treatment (**Fig. 5B**), indicating that AIS remodeling could also rely on protein degradation. A role for the UPS in the AIS proteostasis, as well as for 190-kDa AnkG stability at the spine has previously been reported (*43, 60*). If AnkG is targeted by the UPS, this is not the case for $Na_V1.2$ (**Fig. 4B,C**) and in future studies it would be important to assess the fate of endocytosed $Na_V1.2$ channels. Endocytosed $Na_V1.2$ channels could be targeted to lysosomal degradation or may undergo local recycling, which could provide a 'ready-releasable' recycling pool of Na_V channels, and it is tempting to speculate that such a pool could be used during rapid AIS remodeling. Once endocytosed, the targeting of $Na_V1.2$ for recycling *versus* degradation might rely on the duration and concentration of cytoplasmic Ca^{2+}. In the case of excitotoxic events, the AIS is disrupted in an irreversible manner. Indeed, applying high concentration of glutamate causes the endocytosis and subsequent degradation of AIS $K_V7.2/7.3$ channels, in an NMDAR-dependent manner (*10*). A recent study reports a role for local AIS clathrin-mediated endocytosis of somato-dendritic receptors in the maintenance of neuronal polarity (*26*). In this case, endocytosis is mediated by dynamin1 and internalized receptors are targeted for degradation. It would be interesting to investigate what determines the specificity of the cargos being internalized during basal or activity-driven endocytosis. Here, we observed a change in the distribution of dynamin2 endocytic structures along the AIS during plasticity (**Fig. 5**). Under

basal conditions most of these structures localized to the proximal AIS and we therefore hypothesize that somato-dendritic proteins might be preferentially endocytosed from the proximal AIS (*26*), while AIS plasticity triggers the recruitment of dynamin2 to the distal part of the AIS, inducing internalization of $Na_V1.2$. Moreover, different sets of adaptor proteins might be involved in basal versus activity-driven endocytosis. The adaptor complex protein AP-2 localizes at the AIS and has been implicated in basal endocytosis of somato-dendritic receptors at the AIS (*26*), but it also interacts with $Na_V1.2$ channels (*57*), leaving it open to determine whether other signals might be involved.

Our results suggested that for rapid AIS shortening the temporal coincidence of synaptic activation and postsynaptic depolarization is required: the AnkG-GFP expression remained stable with low-frequency presynaptic stimulation inducing e-LTD, as well as during somatically evoked postsynaptic depolarization with AP firing (**Fig. S5**). While such temporal overlap is experimentally achieved by chemical application of the agonist NMDA (depolarizing spines and dendritic branches as well as the axonal membrane potential and AP generation (this study and (*29*)), whether spike-timing dependent plasticity or other physiologically-relevant stimuli induce rapid AIS plasticity and ion channel endocytosis/insertion remains to be further investigated. Direct experimental evidence for a coincidence detection at the AIS would require triggering in a temporally correlated manner the activation of presynaptic inputs with postsynaptic depolarization and monitor AnkG-GFP. A particularly intriguing possibility is that dendritic NMDA spikes induce AIS plasticity. These large, sustained plateau depolarizations, occurring *in vivo* during sensory integration, locally amplify Ca^{2+} influx and integrate signals from multiple dendrites (*61, 62*). Rapid AIS plasticity mediated by correlated synaptic activation and action potential generation during NMDA spikes may provide a mechanistic explanation for the NMDAR-dependent synergistic scaling of the AP threshold and synaptic responses during long-term potentiation (LTP) (*38*). Our findings with the AnkG-GFP transgenic mouse and Na_V live markers (this study and (*31*)) provide new avenues to experimentally correlate cytoplasmic Ca^{2+} imaging with ion channel membrane dynamics and establish how spatiotemporal patterns of activity-dependent intracellular Ca^{2+} levels links with AIS $Na_V1.2$ membrane endocytosis and insertion. Spike threshold changes are a hallmark of intrinsic plasticity and observed across many species and learning paradigms (*63*). Since activity-dependent changes of the AIS provides a critical hub for short- and long-term intrinsic plasticity, cooperation with synaptic plasticity via common molecular pathways may represent a powerful

mechanism to change the neuronal ensemble activity and engram formation during learning and memory.

Materials and Methods

Animals & Ethics

Double-floxed AnkG-GFP mice (B6;129SV-ank3tm1DCI/HD) were generated by Vann Bennett (previously: Duke University, North Carolina, USA) and Paul Jenkins (University of Michigan, Michigan, USA) and a kind gift by Maren Engelhardt (Johannes-Kepler-University, Linz, Austria). Mice of both sexes were kept at a 12h light-dark cycle (lights on at 07:00, lights off at 19:00) with ad libitum food and water. All animal experiments were performed in compliance with the European Communities Council Directive 2010/63/EU effective from 1 January 2013 and with Dutch national law (Wet op de Dierproeven, 1996). The experiments and ethics were evaluated and approved by the national committee of animal experiments (CCD) applications number AVD 80100 2017 2426 and AVD 80100 2022 16329 (KNAW) and AVD 10800 2017 3404 (Utrecht University). The animal experimental protocols were designed to minimize suffering, approved and monitored by the KNAW animal welfare body (NIN 14.49, NIN 12.13, NIN 20.21.07).

AAV injections

Between 4 to 6 weeks of age mice were anesthetized with isoflurane and head-fixed in a stereotactic apparatus (Kopf instruments). Body temperature was kept at 35 °C with a heating pad. A glass pipette was inserted bilaterally through a small craniotomy (stereotactic coordinates: 3.0 mm P, 3.0 mm L, 2.0-1.5 mm depth). 50 nl of undiluted pENN.AAV.CamKII 0.4.Cre.SV40 (Plasmid #105558, AAV5, Addgene) were injected into the CA1 area of the hippocampus. Cre-recombinase flips the orientation of a cassette containing both the *Ank3* last exon and the coding sequence of eGFP, thus inducing expression of Cre-dependent AnkG-GFP fusion protein. Afterwards the skin was closed with sutures and mice received 1 mg/kg BW meloxicam (Metacam®, Boehringer-Ingelheim, Germany). s.c. as post-operative pain medication. Mice were allowed to recover for at least 2 weeks prior to sacrifice, to allow for sufficient virus expression.

Acute slice preparation

Between 6 to 8 weeks of age, mice were sacrificed for preparation of acute hippocampal brain slices. Mice were deeply anesthetized by application of pentobarbital s.p. (60 mg/kg BW). They were perfused with ice-cold oxygenated cutting artificial cerebrospinal fluid (ACSF, consisting of 125 mM NaCl, 25mM $NaHCO_3$, 1.25 mM NaH_2PO_4, 3 mM KCl, 25 mM Glucose, 1 mM $CaCl_2$, 6 mM $MgCl_2$, and 1 mM kynurenic acid, saturated with 95% O_2 and 5% CO_2, pH 7.4) and subsequently decapitated. The brain was swiftly removed and submerged in ice-cold cutting ACSF (composition see above). 300 µm thick transverse acute hippocampal slices were cut using a Leica VT 1200S vibratome (Leica Biosystems, Wetzlar Germany). Slices were allowed to recover for at least 35 min (60 min for e-LTD experiments) at 35 °C and subsequently kept in a holding chamber at room temperature until experiments commenced. Recordings and incubation experiments were carried out at ~32 °C.

Acute slice plasticity experiments

After sectioning and recovery, the slices were gently transferred onto cell culture inserts (Millicell, 30 mm, Merck) in a small petri dish that was constantly perfused with ACSF (125 mM NaCl, 25 mM $NaHCO_3$, 1.25 mM NaH_2PO_4, 3 mM KCl, 25 mM Glucose, 2 mM $CaCl_2$, 1.3 mM $MgCl_2$ saturated with 95% O_2 and 5% CO_2, pH 7.4) at 6 ml/min. After transfer, the chamber was perfused with 20 µM NMDA (Sigma-Aldrich) in ACSF for 3 minutes, directly followed by perfusion with 100 µM APV (Alfa Aesar) for 3 minutes to prevent prolonged NMDA receptor opening. Control treatment solely consisted of perfusion of slices with 100 µM APV for 3 minutes. Subsequently, slices were fixated using 4% paraformaldehyde (PFA, in 0.1 M PBS) for 20 min at two time-points: before perfusion, as well as after 30 min post treatment. NMDA-treated slices and control slices were taken from corresponding hemispheres at matching CA1 locations (dorsoventral axis) to exclude potential effects of location on AIS length. Slices were then subjected to multichannel immunofluorescent staining. Slices were incubated in blocking buffer (10% normal goat serum [NGS], 1% Triton in 0.1 M phosphate-buffered saline [PBS]) for a minimum of 90 min at room temperature, followed by incubation in primary antibodies overnight (5% NGS, 1% Triton in 0.1 M PBS). Primary and secondary antibodies and concentrations were the same as used for cryosections (see above). Following washing, the slices were incubated with secondary antibodies for a minimum of 4 h in the dark. Streptavidin Alexa-633 conjugate (1:1000; Invitrogen) was added for the detection of biocytin filled neurons. Subsequently, slices were washed and mounted using fluorescence-preserving mounting medium (Vectashield, Vector laboratories). Confocal images of the AIS were acquired using a Leica SP8 confocal microscope (Leica Microsystems, Wetzlar Germany). A

40× objective (oil immersion, NA 1.4) was used for population analysis of AIS length. To ensure that the entire AIS structure was in focus, multiple images in the *z*-dimension were projected to one image (maximum intensity projection). Each image section was spaced at 0.5 µm at a total depth of up to 25 µm. Images were taken at 1024 ´ 1024 resolution, resulting in resolution of 0.27 µm/ pixel. Individual AIS length was determined using the morphometrical software analysis tool AISuite (https://zenodo.org/record/4264831). Segments were individually traced, and the threshold determining start and end of each individual segment was set to be 35% of the maximum fluorescent signal of a single AIS.

Electrophysiology and live AIS imaging

Slices were transferred to an upright microscope (BX61WI, Olympus Nederland BV) and constantly perfused with carbogenated recording ACSF consisting of; 125 mM NaCl, 25 mM $NaHCO_3$, 1.25 mM NaH_2PO_4, 3 mM KCl, 25 mM Glucose. Typically, 2 mM $CaCl_2$, 1.3 mM $MgCl_2$ and 1 mM sodium ascorbate were added while 2.5 mM $CaCl_2$ and 1 mM $MgCl_2$ was used for the e-LTD and depolarisation experiments. The chamber was perfused at a rate of 3 mL/min. Neurons were visualized with a 40× water immersion objective (Achroplan, NA 0.8, IR 40×/0.80 W, Carl Zeiss Microscopy) with infrared optics and oblique contrast illumination. Patch-clamp recordings were performed from CA1 pyramidal neurons with a GFP positive AIS identified during a search in epifluorescence mode and visualizing GFP with the 470 nm laser line of a laser diode illuminator (LDI-7, 89 North, USA). Patch pipettes were pulled from borosilicate glass (Harvard Apparatus, Edenbridge, Kent, UK) pulled to an open tip resistance of 4–5 MΩ and filled with standard intracellular solution containing: 130 mM K-Gluconate, 10 mM KCl, 10 mM HEPES, 4 mM Mg-ATP, 0.3 mM Na_2-GTP, and 10 mM Na_2-phosphocreatine (pH 7.25, ~280 mosmol). For continuous measurements of AP properties over time, we added 1 mM EGTA and 0.1 mM $CaCl_2$ to the standard intracellular solution. Atto-594 (20 µM, Atto-tec, Germany) and biocytin (3 mg/ml, Sigma-Aldrich) were routinely added to the intracellular solution to allow for live- and post-hoc confirmation of colocalization of the AIS with the recorded neuron, respectively. Electrophysiological recordings were performed with an Axopatch 200B (Molecular Devices) or Dagan BVC-700A amplifier (Dagan Corporation, Minneapolis, MN, USA). Signals were analogue low-pass filtered at 10 kHz (Bessel) and digitally sampled at 50 kHz using an A-D converter (ITC-18, HEKA Elektronik Dr. Schulze GmbH, Germany) and the data acquisition software Axograph X (v.1.5.4, Axograph Scientific, NSW, Australia). Bridge-balance and capacitances were fully compensated in current clamp. Series resistance was compensated to > 75% for voltage-clamp recordings. Once a stable

recording was established, AP threshold was recorded at the start (and end) of recordings by injecting 3 ms pulses incrementing 10 pA in amplitude until an AP was generated. In a subset of cells we continuously generated APs every 5 min, in order to correlate length changes with electrophysiological changes over time (**Fig. 6**). For LTD recordings, an extracellular glass bipolar stimulation electrode was positioned above the Schaffer collaterals, to stimulate presynaptic inputs to CA1. The external electrode was tuned to evoke half of the maximum currents in the recorded cell. Initially, > 5 min. of baseline was recorded, and all postsynaptic currents were normalized to the mean evoked current amplitude during baseline. For NMDA induced plasticity experiments, we added 20 µM NMDA (Sigma-Aldrich) for 3 min, similar to previous protocols by (*29, 64*). Since in acute hippocampal slices we observed in some cases excessive irreversible depolarization we subsequently added 100 µM APV (Alfa Aesar) to rapidly antagonize NMDAR-mediated excitation. Control recordings were done with 100 µM APV only. In additional control experiments, we added APV as well as before, during and after NMDA (**Fig. S1E,F**). Neuronal health was further improved by adding sodium ascorbate (1 mM) and increasing $MgCl_2$ (1.0 to 1.3 mM) for the NMDA experiments. AnkG-GFP was imaged using an Olympus FV1000 confocal microscope (Olympus corporation, Tokyo, Japan) controlled by the imaging software FV10-ASW (Ver.03.00). *z*-stacks were acquired at a speed of 12.5 µs/ pixel and a resolution of 800 × 800 pixels in 1 µm steps at 1–3× zoom. To reduce phototoxicity and minimize bleaching the *z*-stacks of AIS were taken at four time points (10 min before and at the start of drug exposure, followed by imaging sessions 30 and 60 min afterwards). For higher temporal resolution imaging (every 5 min, supplementary **movies S1** and **S2**), we used a spinning-disk confocal unit (CSU-X1, Yokogawa) controlled by imaging software Visiview (ver. 5.0.0.28, Visitron systems GmbH, Germany). Images were acquired at 2.3–9 px/µm resolution and 1–4× binning was applied. AIS length was determined with the "Measure ROIs" in Fiji (ImageJ) plugin (https://github.com/cleterrier/Measure_ROIs/blob/56bf5c19c697d1811cc4796588300adeee795c56/Pro_Feat_Fit.js). Fluorescence intensity thresholds for the detection of AIS beginning and end were adjusted between 10% and 35% depending on the signal-to-noise ratio but kept consistent for an individual time series. For some NMDA (n = 12/25) and APV control (n = 8/24) experiments, cells were only imaged but not patched. Multiple neurons per slice were imaged simultaneously to increase data yield. In these cases, healthy neurons were selected based on standard visual criteria (low contrast, no swelling or shrinking).

Primary neuronal cultures and transfection

Primary hippocampal neurons cultures were prepared from embryonic day 18 rat brains (both genders). Cells were plated on coverslips coated with poly-L-lysine (37.5 µg/mL, Sigma-Aldrich) and laminin (1.25 µg/mL, Roche Diagnostics) at a density of 100,000/well of 12-wells plates. Neurons were first cultured in Neurobasal medium (NB) supplemented with 2% B27 (GIBCO), 0.5 mM glutamine (GIBCO), 15.6 µM glutamate (Sigma-Aldrich), and 1% penicillin/streptomycin (GIBCO) at 37 °C in 5% CO_2. From DIV1 onwards, half of the medium was refreshed weekly with BrainPhys medium (BP) supplemented with 2% NeuroCult SM1 neuronal supplement (STEMCELL Technologies) and 1% penicillin/streptomycin. Hippocampal neurons were transfected using Lipofectamine 2000 (Invitrogen). Briefly, DNA (1.8 µg/well, of a 12-wells plate) was mixed with 3.3 µL of Lipofectamine 2000 in 200 µL NB, incubated for 20 min, and then added to the neurons in Neurobasal at 37 °C in 5% CO_2 for 1 hr. Then, neurons were washed with Neurobasal and transferred back to their original medium. Transfection of knock-in constructs was performed at DIV3.

DNA Constructs

The knock-in construct for $Na_V1.2$ was cloned in the pORANGE (*28*) and the gRNA used was: GGACAAAGGGAAAGATATCA. The GFP tag was added in the C-Terminal region (4aa before the STOP codon), mimicking the tagging approach used for $Na_V1.6$ (*23, 65*) or Nav1.2 (*31*), which was shown to not alter channel function nor localization. $Na_V1.2$-GFP and $Na_V1.2$-mCherry over-expression constructs were generated from a $Na_V1.2$-IRES-GFP plasmid shared by Kevin Bender (*66*). The IRES-GFP fragment was cut out using XhoI-PacI restriction sites, and replaced by GFP or mCherry, amplified by PCR, in frame with $Na_V1.2$. Knock-in constructs of GluN1-GFP and clathrin light chain A-GFP (*28*), dynamin2-GFP (*49*), as well as the overexpression construct of dynamin2-GFP (*67*) have previously been published and kindly shared by Dr. MacGillavry (University of Utrecht).

Antibodies

The following antibodies were used in this study: $Na_V1.2$ (NeuroMab/Antibodies Incorporated #75-024), $Na_V1.6$ (Alomone Labs #ASC-009 and NeuroMab/Antibodies Incorporated #73-026), Pan-Nav (Sigma, #S8809), AnkG (Life technologies #33-8800, Neuromab/Antibodies Incorporated #75-146 and Synaptic systems #386-005), βIV-spectrin (Biotrend, provided by Maren Engelhardt, Johnnes-Kepler-University, Linz, Austria), MAP2 (Abcam/Bio Connect #ab5392), GFP (MBL International/Sanbio #598, Abcam #ab13970 and #ab290) and mCherry (Clonthech #632543). Corresponding secondary antibodies Alexa-conjugated 405, 488, 568,

594 or 647 goat anti-mouse, anti-mouse IgG1/IgG2a, anti-rabbit, anti guinea-pig or anti-chicken were used (Life Technologies), as well as streptavidin Alexa-633 conjugate (Life Technologies) for the detection of biocytin filled neurons. Goat anti-mouse and anti-rabbit Abberior Star580 (#ST580) and 635P (#ST635P) were used for STED imaging.

Pharmacological treatments and plasticity experiments

MG-132 (Calbiochem, #474790), MDL 28170 (Tocris Bioscience, #1146/10), MK-801 (Tocris Bioscience, #924), Okadaic Acid (Tocris Bioscience, #1136), Tautomycetin (Tocris Bioscience, #2305), FK-506 (Tocris Bioscience, #3631), Dynasore (Tocris Bioscience, #2897), PitStop2 (Abcam, #ab120687), APV (Tocris Bioscience, #0106), NMDA (Sigma #3263), DHPG (Tocris #0805). All chemicals were diluted in a modified Tyrode's solution (pH 7.4) containing 25 mM HEPES, 119 mM NaCl, 2.4 mM KCl, 2 mM $CaCl_2$, 2 mM $MgCl_2$, 30 mM glucose. For NMDA experiments: neurons were first incubated for 5 min in modified Tyrode's solution, then NMDA 2x (diluted in modified Tyrode's at 100 μM) was added to the wells. For controls experiments Tyrode's solution was applied twice. After 4 min, neurons were dipped in Tyrode's solution to wash them and returned to their original medium. NMDA treatment combined with live imaging was performed the same way, all incubation and washing steps were performed on stage. DHPG experiment: the same procedure was used as for NMDA-LTD, but neurons were incubated for 5 min in 100 μM DHPG. Triton extraction experiment: Live DIV14 hippocampal neurons were incubated for 5 min at RT in 0.25 % Triton X-100 preheated at 37 °C. Neurons were fixed directly after extraction.

Immunocytochemistry

For immunocytochemistry of cultured neurons, cells were fixed for 6 min with warm paraformaldehyde (4%)-sucrose (4%). Primary antibodies were incubated overnight at 4 °C in GDB buffer (0.2% BSA, 0.8 M NaCl, 0.5% Triton X-100, 30 mM phosphate buffer, pH 7.4). After 3 washes in PBS, secondary antibodies were incubated in the same buffer for 1hr at RT. Extracellular staining of GluN1 was performed using a first incubation step with the anti-GFP antibody O/N at 4 °C in GDB without Triton, followed by 3 washes in PBS and incubation with an Alexa568 secondary antibody in GDB without Triton for 2 h at RT. Then anti-GFP and anti-AnkyrinG antibodies were incubated in GDB buffer containing Triton O/N at 4 °C, washed 3 times and corresponding secondary antibodies conjugated with Alexa405 and 647 were incubated in the same buffer for 1 h at RT. Coverslips were mounted using Vectashield (Vectorlabs).

Immunohistochemistry

To examine the expression of AnkG-GFP mice were deeply anesthetized by application of pentobarbital s.p. (60 mg/kg BW) prior to transcardial perfusion with PBS for 5 minutes followed by 4% paraformaldehyde (PFA, in 0.1 M PBS) for 5 minutes. Brains were postfixed in 4% PFA for 1 hour at room temperature (RT). After three sucrose cryoprotection steps (1 h in 10% RT, overnight in 20%, 4 °C, overnight in 30% sucrose, 4 °C) brains were trimmed to sectioning block in coronal orientation and frozen in embedding medium (Tissue-Tek®, Sakura) until further processing. Brains were cut with a cryostat (CM3050 S, Leica) to sections of 40 µm thickness. Slices were incubated in blocking buffer (10% normal goat serum (NGS), 0.5% Triton in 0.1 M PBS) for a minimum of 90 minutes at RT, followed by incubation in primary antibodies overnight (5% NGS, 0.5% Triton in 0.1 M PBS). Following washing steps, the slices were incubated with secondary antibodies for a minimum of 90 minutes in the dark. Subsequently, slices were washed and mounted using fluorescence-preserving mounting medium (Vectashield, Vector laboratories).

Image acquisition

Primary neurons were imaged using a LSM700 confocal laser-scanning microscope (Zeiss) with a Plan-Apochromat 63× NA 1.40 oil DIC, EC Plan-Neofluar 40× NA1.30 oil DIC and a Plan-Apochromat 20× NA 0.8 objective. Z-stacks were acquired with 0.5 µµm steps and maximum projections were done from the resulting stack. Acquisition settings were kept the same for all conditions within an experiment.

gSTED microscopy

Gated STED (gSTED) imaging was performed with a Leica TCS SP8 STED 3X microscope using a HC PL APO 100 × / 1.4 oil immersion STED WHITE objective. The 580, 594, 635 and 647 nm wavelengths of pulsed white laser (80 MHz) were used to excite the Abberior Star 580, Alexa594, Abberior Star 635P and the Alexa647 secondary antibodies. All were depleted with the 775 nm pulsed depletion laser. Fluorescence emission was detected using a Leica HyD hybrid detector with a time gate of $0.3 \leq tg \leq 6$ ns.

Live cell imaging and FRAP experiments

Live-cell imaging experiments were performed in an inverted microscope Nikon Eclipse Ti-E equipped with the perfect focus system (Nikon) and a spinning disk-based confocal scanner unit (CSU-X1-A1, Yokogawa). Plan Apo VC 100x NA 1.40 oil, a Plan Apo VC 60× NA 1.40 oil and a Plan Fluor 40× NA 1.30 oil objectives (all Nikon) were used for acquisition. The system was also equipped with ASI motorized stage with the piezo plate MS-2000-XYZ (ASI), Photometrics PRIME BSI sCMOS camera (Teledyne Photometrics) and controlled by the MetaMorph 7.10 software (Molecular Devices). For imaging we used 100 mW Vortran Stradus 405 laser (Vortran), 150 mW Vortran Stradus 488 laser (Vortran), 100 mW 561 nm OBIS laser (Coherent), and 150 mW Vortran Stradus 642 nm (Vortran) lasers, a set of ET460/50m, ET525/50m, ET630/75m (red) and ET-EGFP/mCherry filters (Chroma) for spinning-disc-based confocal imaging. Optosplit II (Cairn Research) beam splitter was equipped with ET525/50m and ET630/75m emission filters and T585lpxr dichroic mirror (all Chroma). The final resolution using PRIME BSI camera was 0.063 µm/pixel (x100 lens). Coverslips were mounted in metal rings and imaged using a stage top incubator model INUBG2E-ZILCS (Tokai Hit) that maintains temperature and CO_2 optimal for the cells (37 °C and 5% CO_2). Live imaging was performed in full conditioned medium or in imaging buffer. Time-lapse live-cell imaging of $Na_V1.2$ knock-in neurons was performed with a frame rate of 1 acquisition per minute for the FRAP experiments and 1 acquisition every 7.5 minutes for the plasticity experiments. FRAP experiments were carried out with an ILas FRAP unit (Roper Scientific France/ PICT-IbiSA, Institut Curie). Local photobleaching of $Na_v1.2$-GFP in the proximal and distal AIS was performed using ROIs of 30 × 30 pixels (~ 25 μm^2) and recovery was monitored for 45 min, with an image acquisition rate of 1 image per minute. Dynamin2-GFP and $Na_V1.2$-mCherry dual-color imaging was performed with an image acquisition rate of 1 image per 3 seconds.

Image processing and quantification

Movies and images were processed using Fiji (https://imagej.net/software/fiji/) (*68*). Kymographs were generated using the ImageJ plugin from Eugene Katrukha, KymoResliceWide, v0.5, https://zenodo.org/record/4281086. The AIS position (start and end points), length as well as fluorescence intensity of AIS proteins were measured using Christophe Leterrier's plugin 'Pro_Feat_Fit' (https://github.com/cleterrier/Measure_ROIs/blob/56bf5c19c697d1811cc4796588300adeee795c56/Pro_Feat_Fit.js) and with the following parameters: Small detection, starting point at 50% and end-point at 35% of the max fluorescence intensity. The autocorrelation coefficients were obtained using Christophe Leterrier's plugin 'Autocorrelation'

(https://github.com/cleterrier/Process_Profiles/blob/709147ebae553fe58cc20dc5b630271f64f81d73/Autocorrelation_.js). GluN1, Clathrin light chain and Dynamin2 spots quantifications were performed using the Spot Detector plug-in built-in in Icy software (https://icy.bioimageanalysis.org) (*69*). Quantifications parameters were adjusted per experiment but kept similar for all conditions within each experiment. FRAP recovery was quantified as the percentage of fluorescence recovery depending on the initial fluorescence intensity and taking into account the acquisition photobleaching. A bleaching control was selected outside of the bleached areas and fluorescent signals in the ROIs was set to 100% based on the mean intensity of the first 4 frames (4 min) before bleaching in the same region and was set to 0% directly after as described previously (*70*). The average recovery rate was calculated by averaging the values of the last 5 points of fluorescence intensity.

Statistical analysis

All statistical details of experiments, including the exact values of *n*, and statistical tests performed, are provide in the Results, Figures and Figure Legends. *N* represent the number of neurons analyzed, and *N* the number of independent experiments (or animals). All statistical analyses were performed using Prism9 (GraphPad Software). Significance cut-off was defined at 0.05, with ns-not significant, *$p < 0.05$, **$p < 0.01$, and ***$p < 0.001$. Normality of the data was determined by a D'Agostino and Pearson's tests. For comparing two groups parametric two-tailed paired or unpaired t tests or non-parametric Mann Whitney or Wilcoxon tests were used. For more than two groups, one- or two-way ANOVA was applied followed by multiple comparisons tests. When values were missing, a mixed-effects analysis followed by multiple comparisons (specific types are indicated in the text) was applied. For all experiments in cultured neurons, the statistical significance was tested on the average values of each independent experiment when at least 3 independent experiments were performed. For normalized data sets, each value was normalized to the average value of the control condition within the same experiment. Data are plotted as individual values as well as mean ± SD, unless stated differently in the legend.

References

1. M. H. Kole, G. J. Stuart, Signal processing in the axon initial segment. *Neuron* **73**, 235-247 (2012).
2. C. Leterrier, The Axon Initial Segment: An Updated Viewpoint. *J Neurosci* **38**, 2135-2145 (2018).

3. J. J. Garrido *et al.*, A targeting motif involved in sodium channel clustering at the axonal initial segment. *Science* **300**, 2091-2094 (2003).
4. G. Lemaillet, B. Walker, S. Lambert, Identification of a conserved ankyrin-binding motif in the family of sodium channel alpha subunits. *J Biol Chem* **278**, 27333-27339 (2003).
5. N. Jamann *et al.*, Sensory input drives rapid homeostatic scaling of the axon initial segment in mouse barrel cortex. *Nat Commun* **12**, 23 (2021).
6. H. Kuba, Y. Oichi, H. Ohmori, Presynaptic activity regulates Na(+) channel distribution at the axon initial segment. *Nature* **465**, 1075-1078 (2010).
7. E. Galliano *et al.*, Brief Sensory Deprivation Triggers Cell Type-Specific Structural and Functional Plasticity in Olfactory Bulb Neurons. *J Neurosci* **41**, 2135-2151 (2021).
8. H. Kuba, R. Yamada, G. Ishiguro, R. Adachi, Redistribution of Kv1 and Kv7 enhances neuronal excitability during structural axon initial segment plasticity. *Nat Commun* **6**, 8815 (2015).
9. M. S. Grubb, J. Burrone, Activity-dependent relocation of the axon initial segment fine-tunes neuronal excitability. *Nature* **465**, 1070-1074 (2010).
10. T. Benned-Jensen *et al.*, Live Imaging of Kv7.2/7.3 Cell Surface Dynamics at the Axon Initial Segment: High Steady-State Stability and Calpain-Dependent Excitotoxic Downregulation Revealed. *J Neurosci* **36**, 2261-2266 (2016).
11. D. P. Schafer *et al.*, Disruption of the axon initial segment cytoskeleton is a new mechanism for neuronal injury. *J Neurosci* **29**, 13242-13254 (2009).
12. Y. Zhao *et al.*, Calcineurin Signaling Mediates Disruption of the Axon Initial Segment Cytoskeleton after Injury. *iScience* **23**, 100880 (2020).
13. R. H. Roth, Y. Zhang, R. L. Huganir, Dynamic imaging of AMPA receptor trafficking in vitro and in vivo. *Curr Opin Neurobiol* **45**, 51-58 (2017).
14. M. D. Evans *et al.*, Calcineurin signaling mediates activity-dependent relocation of the axon initial segment. *J Neurosci* **33**, 6950-6963 (2013).
15. M. D. Evans, A. S. Dumitrescu, D. L. H. Kruijssen, S. E. Taylor, M. S. Grubb, Rapid Modulation of Axon Initial Segment Length Influences Repetitive Spike Firing. *Cell Rep* **13**, 1233-1245 (2015).
16. S. L. Berger *et al.*, Localized Myosin II Activity Regulates Assembly and Plasticity of the Axon Initial Segment. *Neuron* **97**, 555-570 e556 (2018).
17. A. N. Chand, E. Galliano, R. A. Chesters, M. S. Grubb, A distinct subtype of dopaminergic interneuron displays inverted structural plasticity at the axon initial segment. *J Neurosci* **35**, 1573-1590 (2015).
18. M. D. Evans, C. Tufo, A. S. Dumitrescu, M. S. Grubb, Myosin II activity is required for structural plasticity at the axon initial segment. *Eur J Neurosci* **46**, 1751-1757 (2017).
19. T. Ferreira da Silva *et al.*, Plasmalogens regulate the AKT-ULK1 signaling pathway to control the position of the axon initial segment. *Prog Neurobiol* **205**, 102123 (2021).
20. A. S. Dumitrescu, M. D. Evans, M. S. Grubb, Evaluating Tools for Live Imaging of Structural Plasticity at the Axon Initial Segment. *Front Cell Neurosci* **10**, 268 (2016).
21. C. Leterrier *et al.*, Ankyrin G Membrane Partners Drive the Establishment and Maintenance of the Axon Initial Segment. *Front Cell Neurosci* **11**, 6 (2017).
22. A. Ghosh, E. L. Malavasi, D. L. Sherman, P. J. Brophy, Neurofascin and Kv7.3 are delivered to somatic and axon terminal surface membranes en route to the axon initial segment. *Elife* **9**, (2020).
23. E. J. Akin, L. Sole, S. D. Dib-Hajj, S. G. Waxman, M. M. Tamkun, Preferential targeting of Nav1.6 voltage-gated Na+ Channels to the axon initial segment during development. *PLoS One* **10**, e0124397 (2015).
24. A. Freal *et al.*, Feedback-Driven Assembly of the Axon Initial Segment. *Neuron*, (2019).

25. L. Sole, J. L. Wagnon, E. J. Akin, M. H. Meisler, M. M. Tamkun, The MAP1B binding domain of Nav1.6 is required for stable expression at the axon initial segment. *J Neurosci*, (2019).
26. K. Eichel *et al.*, Endocytosis in the axon initial segment maintains neuronal polarity. *Nature*, (2022).
27. C. Thome *et al.*, Live imaging of excitable axonal microdomains in ankyrin-G-GFP mice. *bioRxiv*, 2023.2002.2001.525891 (2023).
28. J. Willems *et al.*, ORANGE: A CRISPR/Cas9-based genome editing toolbox for epitope tagging of endogenous proteins in neurons. *PLoS Biol* **18**, e3000665 (2020).
29. H. K. Lee, K. Kameyama, R. L. Huganir, M. F. Bear, NMDA induces long-term synaptic depression and dephosphorylation of the GluR1 subunit of AMPA receptors in hippocampus. *Neuron* **21**, 1151-1162 (1998).
30. A. Lorincz, Z. Nusser, Molecular identity of dendritic voltage-gated sodium channels. *Science* **328**, 906-909 (2010).
31. H. Liu, H. G. Wang, G. S. Pitt, Z. J. Liu, Direct Observation of Compartment-Specific Localization and Dynamics of Voltage-Gated Sodium Channels. *J Neurosci*, (2022).
32. C. Leterrier *et al.*, Nanoscale Architecture of the Axon Initial Segment Reveals an Organized and Robust Scaffold. *Cell Rep* **13**, 2781-2793 (2015).
33. H. H. Wong, S. Rannio, V. Jones, A. Thomazeau, P. J. Sjostrom, NMDA receptors in axons: there's no coincidence. *J Physiol* **599**, 367-387 (2021).
34. J. M. Christie, C. E. Jahr, Selective expression of ligand-gated ion channels in L5 pyramidal cell axons. *J Neurosci* **29**, 11441-11450 (2009).
35. E. H. Wong *et al.*, The anticonvulsant MK-801 is a potent N-methyl-D-aspartate antagonist. *Proc Natl Acad Sci U S A* **83**, 7104-7108 (1986).
36. G. N. Woodruff *et al.*, The interaction between MK-801 and receptors for N-methyl-D-aspartate: functional consequences. *Neuropharmacology* **26**, 903-909 (1987).
37. M. J. Palmer, A. J. Irving, G. R. Seabrook, D. E. Jane, G. L. Collingridge, The group I mGlu receptor agonist DHPG induces a novel form of LTD in the CA1 region of the hippocampus. *Neuropharmacology* **36**, 1517-1532 (1997).
38. J. Xu, N. Kang, L. Jiang, M. Nedergaard, J. Kang, Activity-dependent long-term potentiation of intrinsic excitability in hippocampal CA1 pyramidal neurons. *J Neurosci* **25**, 1750-1760 (2005).
39. D. Debanne, Y. Inglebert, M. Russier, Plasticity of intrinsic neuronal excitability. *Curr Opin Neurobiol* **54**, 73-82 (2019).
40. A. Del Puerto *et al.*, ATP-P2X7 Receptor Modulates Axon Initial Segment Composition and Function in Physiological Conditions and Brain Injury. *Cereb Cortex* **25**, 2282-2294 (2015).
41. K. Clark, B. A. Sword, J. L. Dupree, Oxidative Stress Induces Disruption of the Axon Initial Segment. *ASN Neuro* **9**, 1759091417745426 (2017).
42. S. D. Benusa, N. M. George, B. A. Sword, G. H. DeVries, J. L. Dupree, Acute neuroinflammation induces AIS structural plasticity in a NOX2-dependent manner. *J Neuroinflammation* **14**, 116 (2017).
43. M. Lee *et al.*, Ecm29-mediated proteasomal distribution modulates excitatory GABA responses in the developing brain. *J Cell Biol* **219**, (2020).
44. M. P. Fache *et al.*, Endocytotic elimination and domain-selective tethering constitute a potential mechanism of protein segregation at the axonal initial segment. *J Cell Biol* **166**, 571-578 (2004).
45. D. Leyton-Puig *et al.*, Flat clathrin lattices are dynamic actin-controlled hubs for clathrin-mediated endocytosis and signalling of specific receptors. *Nat Commun* **8**, 16068 (2017).

46. E. Macia *et al.*, Dynasore, a cell-permeable inhibitor of dynamin. *Dev Cell* **10**, 839-850 (2006).
47. K. Xu, G. Zhong, X. Zhuang, Actin, spectrin, and associated proteins form a periodic cytoskeletal structure in axons. *Science* **339**, 452-456 (2013).
48. E. D'Este, D. Kamin, F. Gottfert, A. El-Hady, S. W. Hell, STED nanoscopy reveals the ubiquity of subcortical cytoskeleton periodicity in living neurons. *Cell Rep* **10**, 1246-1251 (2015).
49. L. A. Catsburg, M. Westra, A. M. van Schaik, H. D. MacGillavry, Dynamics and nanoscale organization of the postsynaptic endocytic zone at excitatory synapses. *Elife* **11**, (2022).
50. A. Brachet *et al.*, Ankyrin G restricts ion channel diffusion at the axonal initial segment before the establishment of the diffusion barrier. *J Cell Biol* **191**, 383-395 (2010).
51. B. Winckler, P. Forscher, I. Mellman, A diffusion barrier maintains distribution of membrane proteins in polarized neurons. *Nature* **397**, 698-701 (1999).
52. S. Goethals, R. Brette, Theoretical relation between axon initial segment geometry and excitability. *Elife* **9**, (2020).
53. E. C. Beattie *et al.*, Regulation of AMPA receptor endocytosis by a signaling mechanism shared with LTD. *Nat Neurosci* **3**, 1291-1300 (2000).
54. H. Y. Man *et al.*, Regulation of AMPA receptor-mediated synaptic transmission by clathrin-dependent receptor internalization. *Neuron* **25**, 649-662 (2000).
55. M. C. Oh, V. A. Derkach, E. S. Guire, T. R. Soderling, Extrasynaptic membrane trafficking regulated by GluR1 serine 845 phosphorylation primes AMPA receptors for long-term potentiation. *J Biol Chem* **281**, 752-758 (2006).
56. H. K. Lee, K. Takamiya, K. He, L. Song, R. L. Huganir, Specific roles of AMPA receptor subunit GluR1 (GluA1) phosphorylation sites in regulating synaptic plasticity in the CA1 region of hippocampus. *J Neurophysiol* **103**, 479-489 (2010).
57. N. C. Wildburger *et al.*, Quantitative proteomics reveals protein-protein interactions with fibroblast growth factor 12 as a component of the voltage-gated sodium channel 1.2 (nav1.2) macromolecular complex in Mammalian brain. *Mol Cell Proteomics* **14**, 1288-1300 (2015).
58. M. Colledge *et al.*, Ubiquitination regulates PSD-95 degradation and AMPA receptor surface expression. *Neuron* **40**, 595-607 (2003).
59. W. Cheng *et al.*, Proteasomal-Mediated Degradation of AKAP150 Accompanies AMPAR Endocytosis during cLTD. *eNeuro* **7**, (2020).
60. S. Yoon *et al.*, Usp9X Controls Ankyrin-Repeat Domain Protein Homeostasis during Dendritic Spine Development. *Neuron* **105**, 506-521 e507 (2020).
61. J. Schiller, G. Major, H. J. Koester, Y. Schiller, NMDA spikes in basal dendrites of cortical pyramidal neurons. *Nature* **404**, 285-289 (2000).
62. C. Grienberger, X. Chen, A. Konnerth, NMDA receptor-dependent multidendrite Ca(2+) spikes required for hippocampal burst firing in vivo. *Neuron* **81**, 1274-1281 (2014).
63. W. Zhang, D. J. Linden, The other side of the engram: experience-driven changes in neuronal intrinsic excitability. *Nat Rev Neurosci* **4**, 885-900 (2003).
64. A. Kamal, G. M. Ramakers, I. J. Urban, P. N. De Graan, W. H. Gispen, Chemical LTD in the CA1 field of the hippocampus from young and mature rats. *Eur J Neurosci* **11**, 3512-3516 (1999).
65. A. Gasser *et al.*, An ankyrinG-binding motif is necessary and sufficient for targeting Nav1.6 sodium channels to axon initial segments and nodes of Ranvier. *J Neurosci* **32**, 7232-7243 (2012).

66. R. Ben-Shalom *et al.*, Opposing Effects on NaV1.2 Function Underlie Differences Between SCN2A Variants Observed in Individuals With Autism Spectrum Disorder or Infantile Seizures. *Biol Psychiatry* **82**, 224-232 (2017).
67. N. Scheefhals *et al.*, Shank Proteins Couple the Endocytic Zone to the Postsynaptic Density to Control Trafficking and Signaling of Metabotropic Glutamate Receptor 5. *Cell Rep* **29**, 258-269 e258 (2019).
68. J. Schindelin *et al.*, Fiji: an open-source platform for biological-image analysis. *Nat Methods* **9**, 676-682 (2012).
69. F. de Chaumont *et al.*, Icy: an open bioimage informatics platform for extended reproducible research. *Nat Methods* **9**, 690-696 (2012).
70. R. D. Phair, S. A. Gorski, T. Misteli, Measurement of dynamic protein binding to chromatin in vivo, using photobleaching microscopy. *Methods Enzymol* **375**, 393-414 (2004).

Acknowledgments

The authors are indebted to the support by the neuron culture team and the imaging facility at Utrecht University. We would like to thank Dr. Harold MacGillavry (Utrecht University) for the great discussions, help throughout the project and for sharing many of the constructs. We also thank Dr. Kevin Bender (UCSF) for sharing the $Na_V1.2$-IRES-GFP construct.

Funding:

The Netherlands Research Council NWO Vici 865.17.003 (MK)

The Netherlands Research Council NWO Veni.192.242 (AF)

Author contributions:

Conceptualization: AF

Methodology: AF, MHPK, NJ

Investigation: AF, NJ, JTB, JJ, TL, NP

Visualization: AF, NJ, MHPK

Funding acquisition: AF, MHPK

Project administration: AF, MHPK

Supervision: AF, MHPK, NJ

Writing – original draft: AF, NJ, MHPK

Writing – review & editing: AF, NJ, MHPK, CCH

Competing interests:

C.C.H. is an employee of Genentech, Inc., a member of the Roche group.

Data and materials availability:

All data are available in the main text or the supplementary materials. All the constructs generated in this study are available upon request to the corresponding authors. Permanent links to all codes used in this study can be found in the Materials and Methods.

Supplementary Materials

Figures S1 to S9

Movies S1 to S2